LANGMUIR

pubs.acs.org/Langmuir Article

Porous Photo-Fenton Catalysts Rapidly Triggered by Levodopa-Based Mussel-Inspired Coatings for Enhanced Dye Degradation and Sterilization

Shang-Jin Yang,[§] Zhi-Yuan Xu,[§] Ling-Yun Zou,[§] Jiong-Chi Yu, Jian Ji,* and Zhi-Kang Xu*

Cite This: *Langmuir* 2022, 38, 9587−9596 Read Online

ACCESS | Metrics & More | Article Recommendations | Supporting Information

ABSTRACT: The advanced oxidation process of the photo-Fenton reaction can produce hydroxyl radicals with extremely strong oxidizing properties for the efficient and green degradation of various chemical and microbial pollutants. Herein, we report an approach to fabricating heterogeneous Fenton catalysts of β-FeOOH nanorods on porous substrates triggered by mussel-inspired coatings of levodopa (3,4-dihydroxy-phenyl-L-alanine, L-DOPA) and polyethylenimine (PEI) for efficient photocatalytic dyes' degradation and sterilization. The L-DOPA-based coatings not only promote the formation and immobilization of β-FeOOH nanorods on the porous substrates by strong coordination between catechol/carboxyl groups and Fe^{3+} but also improve the energy band structure of the Fenton catalysts through a valence band blue shift and band gap narrowing. The photo-Fenton catalysts prepared by the L-DOPA-based coatings exhibit high electron transport efficiency and improved utilization of sunlight. Only 2 h of mineralization is needed to fabricate these catalysts with excellent photocatalytic efficiency, in which the degradation efficiency of methylene blue can reach 99% within 30 min, whereas the sterilization efficiency of *E. coli*/*S. aureus* can reach 93%/94% within 20 min of the photo-Fenton reaction. Additionally, the prepared catalysts reveal a high photodegradation performance for various dyes including methylene blue, methyl blue, methyl orange, direct yellow, and rhodamine B. Furthermore, the catalysts retain high dye degradation efficiencies of above 90% after five photodegradation cycles, indicating cycling performance and good stability.

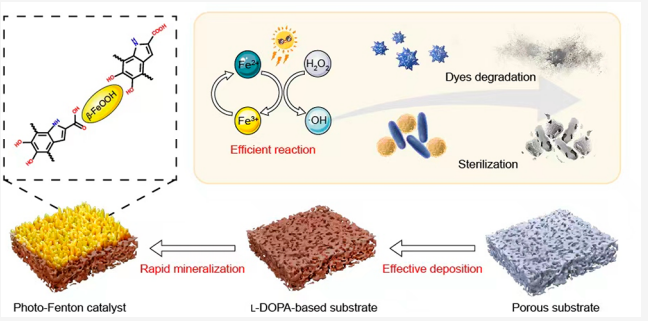

INTRODUCTION

Water pollution caused by population expansion and industrial development has been a worldwide issue for more than a century.[1] Chemical and microbial contaminants are always the focus of water pollution control because of the complexity of their compositions, which are difficult to separate and degrade, and the severity of the harm they cause through subsequent eutrophication of water bodies.[2,3] Various technologies have been developed for wastewater treatment, mainly including physical adsorption,[4,5] chemical oxidation,[6−8] and biological degradation.[9,10] Among those chemical methods, the photo-Fenton reaction has attracted increased attention because of its high treatment efficiency and visible light utilization as well as mild reaction conditions.[11−14] In a typical photo-Fenton process, Fe^{2+} reacts with H_2O_2 to form hydroxyl radicals and Fe^{3+} ions under ultraviolet and visible light irradiation. The hydroxyl radicals are strong oxidizers that can degrade various organic pollutants in wastewater effectively. However, Fe^{3+} ions can precipitate out of the aqueous solutions easily, which will cause the loss of the photo-Fenton catalyst and result in an attenuated photodegradation ability and secondary pollution.[15] To overcome these obstacles, much effort has been expended to develop heterogeneous Fenton catalysts as Fe^{2+} sources. These Fe^{2+} sources are usually anchored on substrates to realize the good recovery and recycling of Fenton catalysts, and this would lead to a reduction in the specific surface area of the Fenton reaction and thus impaired photocatalytic activity.[16−20] Therefore, it remains a challenge to immobilize the Fe^{2+} sources on porous substrates with high specific surface areas and simultaneously improve the photodegradation efficiency and recycling durability during the photo-Fenton process.

The mussel-inspired chemistry of catechol derivatives provides a facile method to modify porous substrates and then to mineralize β-FeOOH nanorods as heterogeneous photo-Fenton catalysts for dye degradation.[21,22] In these cases, the catechol groups in dopamine-based mussel-inspired coatings can offer mineralization sites for the formation of β-FeOOH nanorods on porous substrate surfaces. However, the whole preparation process is tedious because the formation of

Received: April 19, 2022
Revised: July 18, 2022
Published: July 26, 2022

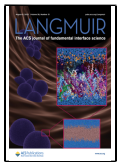

https://doi.org/10.1021/acs.langmuir.2c00999
Langmuir 2022, 38, 9587−9596

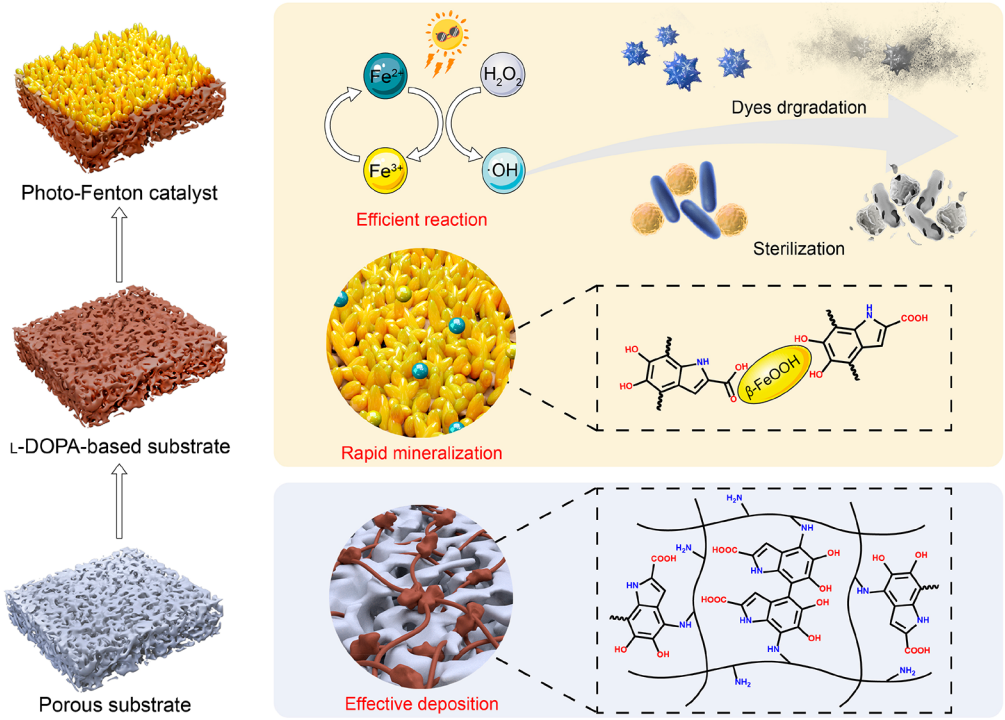

Figure 1. Schematic illustration of the fabrication process and photocatalytic mechanism of the prepared photo-Fenton catalysts.

mussel-inspired coatings was conducted for 4 h and the mineralization of β-FeOOH should be carried out for 24−48 h. Moreover, the influencing mechanism of the mussel-inspired coatings on the photo-Fenton reaction of β-FeOOH nanorods is still not well understood.

In fact, mussel-inspired coatings can be rapidly constructed on a variety of material surfaces by the codeposition of levodopa (L-DOPA, 3,4-dihydroxyphenyl-L-alanine) and polyethylenimine (PEI).[23,24] These L-DOPA-based mussel-inspired coatings can be further applied as bridges to firmly bond the substrate surfaces with inorganic nanomaterials via the strong coordination of carboxyl and catechol groups with metal ions.[25−28] Moreover, the coatings are composed of 5,6-dihydroxyindole-2-carboxylic acid (DHICA), which has better free-radical-scavenging properties than does 5,6-dihydroxyindole (DHI) in dopamine-based coatings. The DHICA moieties can be expected to serve as electron-transfer intermediates to enhance the photocatalytic efficiency of Fenton catalysts.[29−31] Herein, we report porous photo-Fenton catalysts rapidly triggered by L-DOPA-based mussel-inspired coatings for enhanced dye degradation and sterilization (Figure 1). In our case, L-DOPA is quickly cross-linked with PEI to form mussel-inspired coatings on microporous polypropylene substrate. The great quantity of carboxyl and catechol groups in the L-DOPA-based coatings provides effective mineralization sites for β-FeOOH nanorods and enhances the interface stability of the photo-Fenton catalyst and the porous substrate. The mineralization process can be significantly shortened from 24−48 to 2−6 h. Furthermore, as a good electron acceptor, the L-DOPA-based coatings optimize the energy band structure of the photocatalyst, enhancing the efficiencies of sunlight utilization and electron transmission and finally promoting the photo-Fenton reaction. Ultimately, the prepared heterogeneous Fenton catalysts exhibit excellent photocatalytic activity with good structural stability for degrading various dyes and killing bacteria in wastewater under sunlight.

EXPERIMENTAL SECTION

Materials. The porous substrate was a polypropylene microfiltration membrane with an average pore size of 0.2 μm and a porosity of 75%, purchased from Membrana GmbH (Germany). L-DOPA, PEI (Mw = 600 Da), and coumarin were purchased from Shanghai Aladdin Chemistry Co. Ltd. (China). *Staphylococcus aureus* (*S. aureus*, ATCC 29213) and *Escherichia coli* (*E. coli*, ATCC 8739) were obtained from the Guangdong Culture Collection Center (China). Tryptic soy broth, tryptic soy agar, lysogeny broth (LB), and LB nutrient agar were purchased from Basebio (China). Other chemicals, including iron chloride hexahydrate ($FeCl_3{\cdot}6H_2O$), hydrochloric acid (HCl, 38%), H_2O_2 (30% in water), methylene blue, rhodamine B, methyl blue, methyl orange, direct yellow, and ethanol, were commercially provided by Sinopharm Chemical Reagent Co. Ltd. (China).

Fabrication of L-DOPA/PEI-Functionalized Substrates. L-DOPA was dissolved in Tris buffer (pH = 8.5, 50 mmol/L) at a fixed concentration of 2.0 mg/mL at room temperature. PEI was then added to these solutions with different L-DOPA/PEI ratios. The porous substrates with a round diameter of 3.5 cm were immersed in 15.0 mL of an L-DOPA/PEI solution and shaken at 25 °C for 4 h to fabricate the L-DOPA-based mussel-inspired coatings. The substrates were then washed with deionized water and dried in a vacuum oven at 35 °C for 8 h.

β-FeOOH Mineralization on Porous Substrates. $FeCl_3{\cdot}6H_2O$ (0.07 M) was dissolved in a mixed solution of deionized water (10 mL) and hydrochloric acid (5 mL, 0.01 M). Then, one piece of the porous substrates was immersed in this solution for 1 to 12 h at 60 °C. Subsequently, the prepared β-FeOOH catalysts were rinsed with deionized water three times and dried in a vacuum oven at 35 °C for 8 h.

The β-FeOOH catalyst without L-DOPA-based coatings is labeled 0:0. Those triggered by L-DOPA-based coatings prepared from different L-DOPA/PEI concentration ratios are labeled *X*:*X*. β-FeOOH catalysts triggered by L-DOPA-based coatings prepared from an L-DOPA/PEI concentration ratio of 2:1 but various mineralization times are labeled *X* h.

Characterization. The surface morphologies were visualized by a field-emitting scanning electron microscope (FESEM, Hitachi S4800,

https://doi.org/10.1021/acs.langmuir.2c00999
Langmuir 2022, 38, 9587−9596

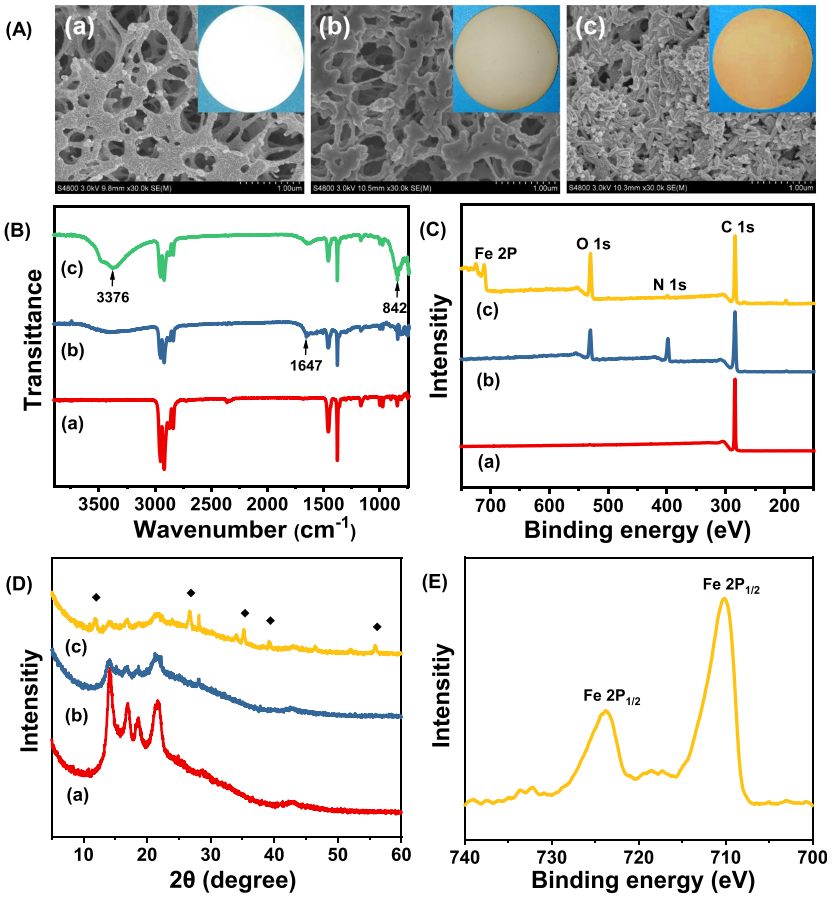

Figure 2. (A) Surface morphologies, (B) ATR/FT-IR spectra, (C) XPS spectra, and (D) XRD patterns of the (a) nascent, (b) L-DOPA/PEI-functionalized substrates, and (c) β-FeOOH catalysts triggered by L-DOPA-based coatings. (E) High-resolution XPS spectra of the Fe 2p core level on the studied β-FeOOH catalysts. (The L-DOPA concentration was fixed at 2.0 mg/mL, the L-DOPA/PEI concentration ratio was kept at 2:1, the deposition was conducted for 4 h at room temperature, and the mineralization process was carried out for 6 h at 60 °C.)

Japan) after being sputtered with a 15−25 nm gold layer on the sample surface. The attenuated total reflectance Fourier transform infrared spectra were recorded on an infrared spectrophotometer equipped with an ATR accessory (ATR/FT-IR, Nicolet 6700, USA). The crystallization phase of the mineralized β-FeOOH nanorods was analyzed by X-ray diffraction (XRD, Empyrean 200895, The Netherlands). The chemical constitutions of prepared samples were determined by X-ray photoelectron spectroscopy (XPS, PerkinElmer, USA). The total density of states (DOS) of the studied catalysts was measured by valence-band XPS spectra (VB-XPS, Thermo Scientific K-Alpha, USA). The dynamic contact angles were detected using a DropMeter A-200 contact angle system (MAIST Vision Inspection & Measurement Co. Ltd., China). The zeta potentials of the substrate surfaces were measured on an electrokinetic analyzer (SurPASS Anton Paar, GmbH, Austria). UV−vis diffuse reflectance spectra (DRS), by which the band gaps of β-FeOOH catalysts were calculated, were recorded on a UV−vis spectrophotometer (UV2550, Shimadzu, China) by using $BaSO_4$ as the reference. A photoluminescence spectrometer (FLS920, Edinburgh Instruments) with a Xe lamp (450 W, 325 nm) as the excitation source was used.

Evaluation of the Hydroxyl Radical (·OH) Generation Ability. The ability of the studied catalysts to generate ·OH was detected by fluorescence (FL) using coumarin (COU) as a probe molecule. COU can react with ·OH to produce highly fluorescent product 7-hydroxycoumarin (7HC), which exhibits a FL signal at 456 nm. Hydrochloric acid, hydrogen peroxide, and COU were dispersed in distilled water to obtain an aqueous solution (pH = 3, $[H_2O_2]$ = 10 mM, and [COU] = 500 μM). One milliliter of the solution was then added to a 24-well culture plate for each sample, and a Xe lamp (450 W) was used as a simulated sunlight source 20 cm above the dishes. The FL intensities of 7HC (Ex = 332 nm, Em = 456 nm) were detected by a spectrofluorophotometer (RF-5301PC, Shimadzu).

Evaluation of the Photocatalytic Degradation Efficiency. First, various dyes, including methylene blue, rhodamine B, methyl blue, methyl orange, and direct yellow, were dissolved in deionized water at a concentration of 20 mg/L. The solutions were acidified with sulfuric acid to a pH of 3 to prepare the dyed wastewater. Then, the porous catalyst was immersed in 25 mL of dyed wastewater at room temperature for 30 min. Next, the initial dye concentration (C_0) was measured by UV−vis spectrophotometry. After 2.5 μL of H_2O_2 was added, the dyed wastewater containing the studied catalyst was exposed to visible light (450 W Xe lamp) for a series of reaction times at room temperature, and the dye concentration (C_t) was measured again. Finally, the photocatalytic degradation efficiency of the corresponding material was calculated by C_t/C_0 for each dye.

Bacterial Culture. *S. aureus* and *E. coli* were employed as representative Gram-positive and Gram-negative bacteria, respectively. A single colony of bacteria was transferred into media while shaking (120 rpm) at 37 °C; the samples were shaken overnight until the OD_{600} reached 0.1, which indicated that the bacterial growth was in the logarithmic phase (10^8 CFU/mL).

Photocatalytic Antibacterial Assay. According to a previous antibacterial assay, individual catalysts (square pieces with a side length of 1 cm) were fixed on the bottom of a 24-well culture plate. PBS solution (pH = 5.0, $[H_2O_2]$ = 100 μM) was prepared via the addition of hydrochloric acid and hydrogen peroxide. The bacterial medium that was cultured overnight was diluted with the prepared PBS solution (1×10^5 CFU/mL), and 1 mL of the bacterial suspension was added to completely cover each porous catalyst. After treatment with 20 min of illumination by a Xe lamp and incubation at

https://doi.org/10.1021/acs.langmuir.2c00999
Langmuir 2022, 38, 9587−9596

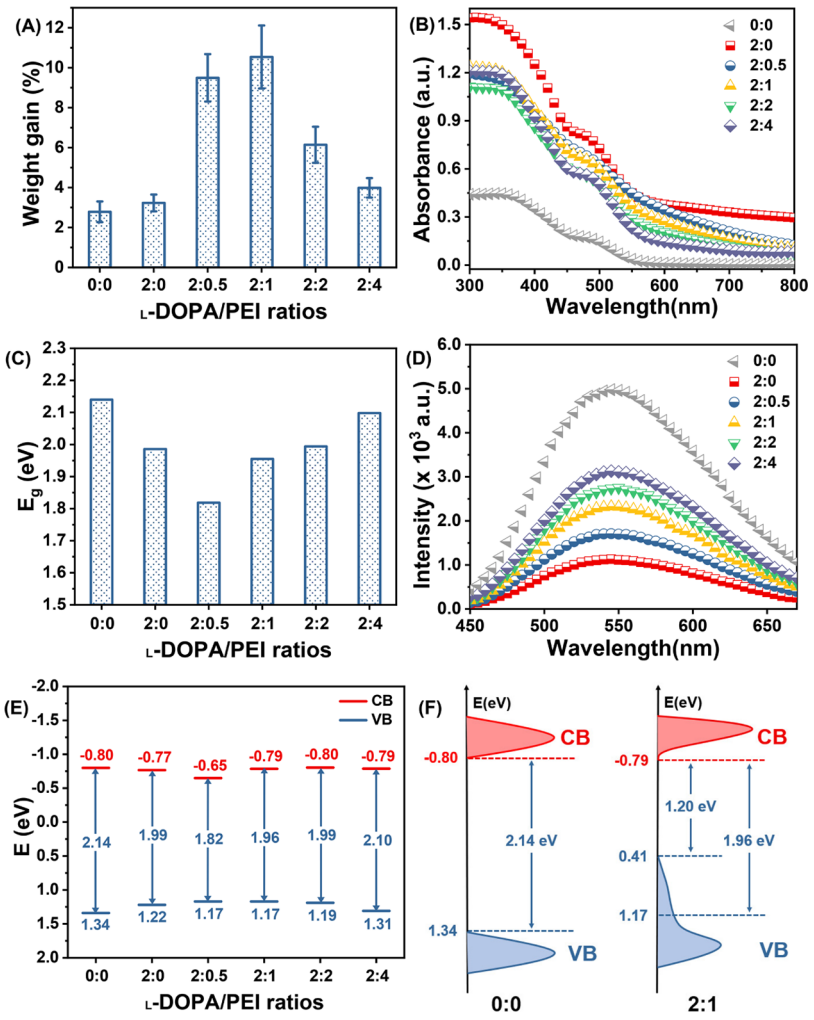

Figure 3. (A) Mineralization weight gain, (B) UV−visible diffuse reflectance spectra, and (D) photoluminescence emission spectra of the β-FeOOH catalysts triggered by L-DOPA-based coatings prepared from different L-DOPA/PEI concentration ratios. (C) The energy band gap and (E) density of states (DOS) were calculated on the basis of the UV−visible diffuse reflectance spectra and the VB-XPS results. (F) Schematic illustration of the DOS of L-DOPA-based photocatalysts compared to that of the unmodified β-FeOOH. (The materials were prepared similarly to those in Figure 2.)

37 °C for 6 h, the bacterial suspension was serially diluted. Then, the diluted samples (100 μL) were spread on agar plates. After another incubation at 37 °C for 18 h, the colonies that formed were simultaneously counted and recorded using a digital camera.

RESULTS AND DISCUSSION

The surface morphologies were visualized by FESEM for the studied substrates and the prepared porous photo-Fenton catalysts. Figure 2A and Figure S1 in the Supporting Information show that the substrate surfaces vary little by immersion in the aqueous L-DOPA solution for 4 h. In contrast, uniform L-DOPA-based coatings are facilely formed on the substrate surfaces when 0.5−1.0 mg/mL PEI was added to the L-DOPA solution for codeposition (Figure 2A and Figure S2 in the Supporting Information). However, the L-DOPA-based coatings become thinner with the PEI concentration increasing from 2.0 to 4.0 mg/mL. Then β-FeOOH nanorods gradually form and are uniformly immobilized on the porous substrates with L-DOPA-based coatings when the mineralization time is extended from 1 to 6 h (Figure 2A and Figure S3 in the Supporting Information). If the mineralization time is further prolonged to 12 h, then the substrate pores are blocked by β-FeOOH nanorods, which is detrimental to the heterogeneous photo-Fenton reaction.

ATR/FT-IR, XPS, and XRD were used to analyze the chemical structures and crystallization phases of the prepared samples. The ATR/FT-IR spectra (Figure 2B and Figure S4 in the Supporting Information) show peaks at 2950 and 1457 cm^{-1}, which are owing to the C−H stretching vibration and the bending vibration of the nascent substrate. New peaks arise at 1647 and 3376 cm^{-1} after L-DOPA/PEI functionalization. The peak at 1647 cm^{-1} is ascribed to the carbon−nitrogen double bonds between L-DOPA and PEI, and the peak at 3376 cm^{-1} is due to the hydroxyl stretching vibration in L-DOPA. Compared with the L-DOPA/PEI-functionalized substrates, the samples with β-FeOOH exhibit a new peak at 837 cm^{-1}, which is ascribed to the Fe−O stretching vibration in β-FeOOH nanorods, and the peak of hydroxyl at 3376 cm^{-1} is reinforced notably. The XPS spectra (Figure 2C) show that there is only a C 1s characteristic peak in the nascent substrate, N and O absorption peaks appear in the L-DOPA-based substrate, and a new Fe 2p characteristic peak appears after β-FeOOH mineralization. Additionally, in the high-resolution XPS spectra of the L-DOPA-based substrates, the C 1s peak

https://doi.org/10.1021/acs.langmuir.2c00999
Langmuir 2022, 38, 9587−9596

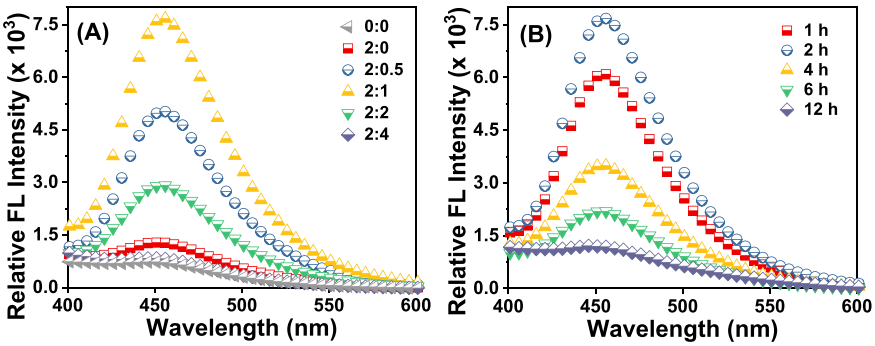

Figure 4. (A and B) ·OH generation efficiency of the β-FeOOH catalysts with L-DOPA-based coatings prepared from different L-DOPA/PEI concentration ratios and mineralization times (comparison of FL intensity for different samples in 500 μM COU aqueous solution under 10 min of sunlight irradiation).

shifts to higher binding energy, indicating the formation of carbon−nitrogen double bonds and the carbon−nitrogen single bonds formed via Schiff-base reactions and Michael additions between L-DOPA and PEI (Figure S5 in the Supporting Information). Meanwhile, the characteristic peaks of the Fe $2p_{1/2}$ and Fe $2p_{3/2}$ orbitals can be identified from the β-FeOOH catalysts (Figure 2E). The XRD patterns (Figure 2D) indicate four peaks at 14.0, 16.8, 18.6, and 21.7° from the nascent substrate, and no new peaks can be found in the pattern of the L-DOPA-based substrate. Instead, the standard diffraction peaks of β-FeOOH (JCPDS card 34-1266) appear at 11.9, 26.9, 35.3, 39.4, and 56.3° from the studied catalyst surface. These results reveal the efficient mineralization and the stable immobilization of β-FeOOH nanorods on the L-DOPA-based substrates.

The constructed photo-Fenton catalysts are revealed by the weight gains of β-FeOOH mineralization. Figure 3A shows that there is little weight gain (about 2.8%) when the mineralization is carried out on the nascent substrate without L-DOPA-based coatings (0:0). However, the mineralization process is greatly improved to a 10.5% weight gain by the mussel-inspired coatings prepared from the L-DOPA/PEI concentration ratio of 2:1. This improvement is ascribed to the abundant active carboxyl and catechol groups in the L-DOPA-based coatings, which can significantly change the properties of the substrate surfaces (Figure S6 and Table S1 in the Supporting Information) while providing mineralization sites for the Fenton catalysts. On the other hand, the mineralization promotion gradually becomes invalid as the PEI concentration in the codeposition solution increases from 2.0 to 4.0 mg/mL (2:2 and 2:4). This occurs because the β-FeOOH nanorods are immobilized on the L-DOPA-based coatings through coordination bonds between the Fe^{3+} ions and the carboxyl and catechol groups, during which the charge repulsion between the amino groups and Fe^{3+} ions may hinder this immobilization reaction. This trend is also demonstrated by the surface zeta potentials of the substrates (Figure S6 in the Supporting Information). Finally, the mineralization results (Figure 3A) reveal that the ideal concentration ratio of L-DOPA/PEI is 2:1 for fabricating L-DOPA-based coatings because the intermediate coating possesses relatively high reactive groups and low positive charges, which are favorable for the immobilization and growth of β-FeOOH nanorods. It is worth noting that the immobilized amount of β-FeOOH catalysts increases with the mineralization time, and 6 h is sufficient to form a continuous β-FeOOH layer on the substrates (Figure S7 in the Supporting Information).

As a photo-Fenton catalyst, β-FeOOH has a narrow energy band gap (E_g = 2.12 eV) to achieve an effective response to visible light. It is known that improving the utilization efficiency of sunlight (visible light accounts for 46% and ultraviolet light accounts for 5%) can effectively improve the photo-Fenton degradation performance.[32,33] The UV−visible diffuse reflectance spectra (Figure 3B) show that the introduction of the melanin-like L-DOPA-based coatings could enhance the ultraviolet (wavelength approximately 200−400 nm) and visible light (wavelength greater than 400 nm) absorption of the prepared β-FeOOH catalysts significantly. Meanwhile, the maximum optical absorption threshold (λg) of the β-FeOOH catalysts with L-DOPA-based coatings shifts to longer wavelengths (red shift), revealing the reduction of the energy band gap and the expansion of the response range to visible light.[34] As shown in Figure 3C, the band gap of the β-FeOOH catalyst without the mussel-inspired coatings (0:0) is approximately 2.14 eV, which is basically consistent with the reported value of 2.12 eV. After the introduction of the L-DOPA-based coatings, the energy band gaps of the prepared photocatalysts decrease to 1.99 (2:0), 1.82 (2:0.5), 1.96 (2:1), 1.99 (2:2), and 2.10 eV (2:4). In addition, Figure 3D indicates that the photoluminescence intensity of the β-FeOOH catalysts decreases with increasing L-DOPA content in the L-DOPA/PEI intermediate coatings. This result reveals that our L-DOPA-based coatings could act as the electron acceptor to reduce the electron−hole recombination rate and improve the electron transport efficiency.[35]

The total density of states (DOS) of the prepared samples was measured by valence-band XPS (VB-XPS).[36,37] Figure 3F and Figure S8 in the Supporting Information show that the catalyst without L-DOPA-based coatings (0:0) displays typical DOS characteristics of β-FeOOH with a valence band edge at about 1.34 eV. After introducing the L-DOPA-based coatings (2:1), the valence band blue shifts toward the vacuum energy level with a band tail state extending toward the conduction band. The main absorption onset of the valence band is located at 1.17 eV, and the valence band tail is located at 0.41 eV. This result is attributed to the electron-delocalization ability of carboxyl ligands and the electron-transfer ability of the indole structures (DHI and DHICA) in L-DOPA-based coatings.[22,29] Furthermore, the conduction band positions were calculated using the numerical results of the energy band gaps and the valence band maximum energy edges (Figures S8 and S9 in the Supporting Information). As shown in Figure 3E,F, the L-DOPA-based coatings cause band gap narrowing of the β-FeOOH catalysts due to the blue shift of the valence band

https://doi.org/10.1021/acs.langmuir.2c00999
Langmuir 2022, 38, 9587−9596

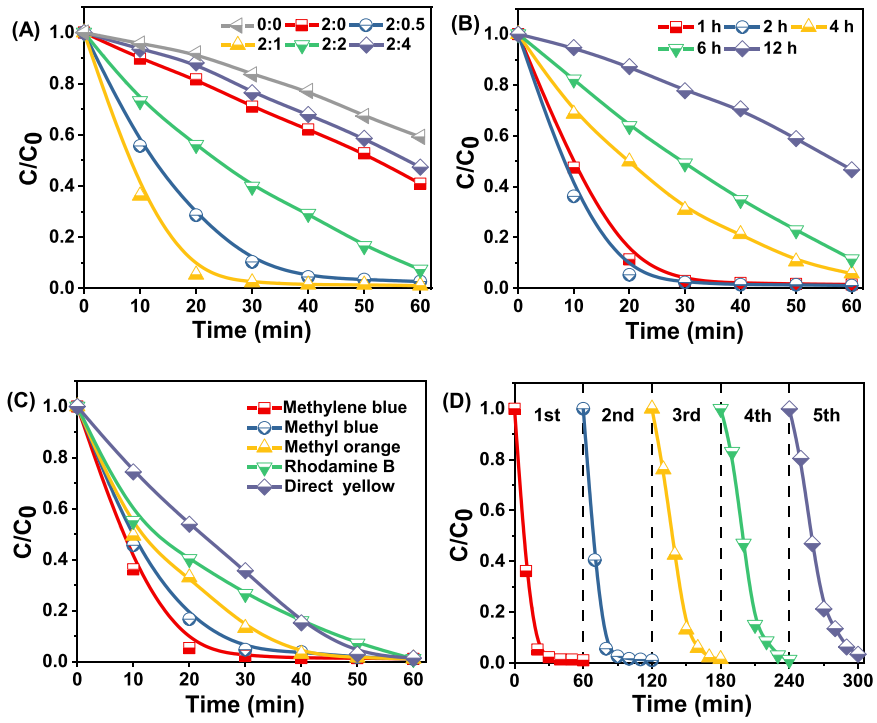

Figure 5. (A and B) Photodegradation of methylene blue in the presence of β-FeOOH catalysts with L-DOPA-based coatings prepared from different L-DOPA/PEI concentration ratios and mineralization times. (C) Photodegradation of different dye solutions in the presence of β-FeOOH catalysts. (D) Reusability of β-FeOOH catalysts for the degradation of methylene blue. (The L-DOPA/PEI concentration ratio was maintained at 2:1, and the mineralization time was maintained at 2 h.)

edge and the extension of the valence band tail, which will effectively promote the separation of current carriers while improving the electron transport. In general, the L-DOPA-based coatings can effectively improve the energy band structure of the β-FeOOH catalyst and enhance the photo-Fenton reaction ability.

The photocatalytic performance of β-FeOOH depends on the production of reactive oxygen radicals (ROS) during the Fenton process.[33] In this study, coumarin was used as a micromolecule fluorescent probe to detect the hydroxyl radicals (·OH), and the relative fluorescence intensity of 7-hydroxycoumarin was measured by fluorescence spectroscopy to determine the ·OH generation efficiency of the studied catalysts during the photo-Fenton reaction.[38] Figure 4A demonstrates that the introduction of the L-DOPA-based coatings significantly increases the ·OH generation efficiency during the photo-Fenton process. This efficiency satisfies the sequence 2:1 > 2:0.5 > 2:2 > 2:0 > 2:4 > 0:0 for the prepared β-FeOOH catalysts. Figure 4B reveals that the maximum ·OH radical generation efficiency is achieved with only 2 h of mineralization, and further increasing the mineralization time will gradually reduce the free radical production efficiency. This is because the β-FeOOH catalyst mineralized for 2 h exhibits a narrower energy band gap and a lower electron−hole recombination rate than the catalyst mineralized for 6 h (Figure S10 in the Supporting Information). Additionally, when the mineralization time increases further, the excess β-FeOOH nanorods block the pores of the substrates obviously, leading to a reduction in the active specific surface area and an impairment of the photocatalytic efficiency. Moreover, shorter mineralization times lead to more defects in the catalyst crystal, and it has been reported that the defects in the crystal itself can also improve the photocatalytic performance.[39]

The prepared β-FeOOH catalysts were applied to the photocatalytic degradation of dyes in water through the photo-Fenton reaction. Figure 5A indicates that the photodegradation efficiency for methylene blue is only 16% within 30 min and 41% within 60 min when using the β-FeOOH catalyst without L-DOPA-based coatings (0:0) under simulated sunlight irradiation. However, it increases sharply to 99% within 30 min when using the β-FeOOH catalyst with L-DOPA-based coatings fabricated at a concentration ratio of 2:1. These results demonstrate that the L-DOPA-based mussel-inspired coatings are able not only to immobilize β-FeOOH nanorods stably but also to enhance the photocatalytic activity of the Fenton catalysts remarkably. In addition, we investigated the effect of the L-DOPA/PEI ratio and mineralization time on the photocatalytic efficiency of the prepared catalysts (Figure 5A,B, Figure S11 in the Supporting Information). There is a good corresponding relationship between the degradation efficiency of dyes and the generation efficiency of ·OH. These results show that the optimum photocatalytic performance can be achieved when the L-DOPA-based coating is fabricated from an L-DOPA/PEI concentration ratio of 2:1 within 2 h of mineralization. Compared with our previous work,[21,22] the mineralization time of the β-FeOOH nanorods can be shortened from 24 to 2 h, and the photo-Fenton reaction time can also be compressed from 60 to 30 min to achieve as high as 99% dye degradation efficiency. Furthermore, we also compared the ROS production efficiency and the photodegradation ability of the β-FeOOH catalysts prepared by PDA-based coatings under the same condition. The Fenton catalysts prepared by the L-DOPA-based coatings exhibit significant advantages (Figure S12 in the Supporting Information).

https://doi.org/10.1021/acs.langmuir.2c00999
Langmuir 2022, 38, 9587−9596

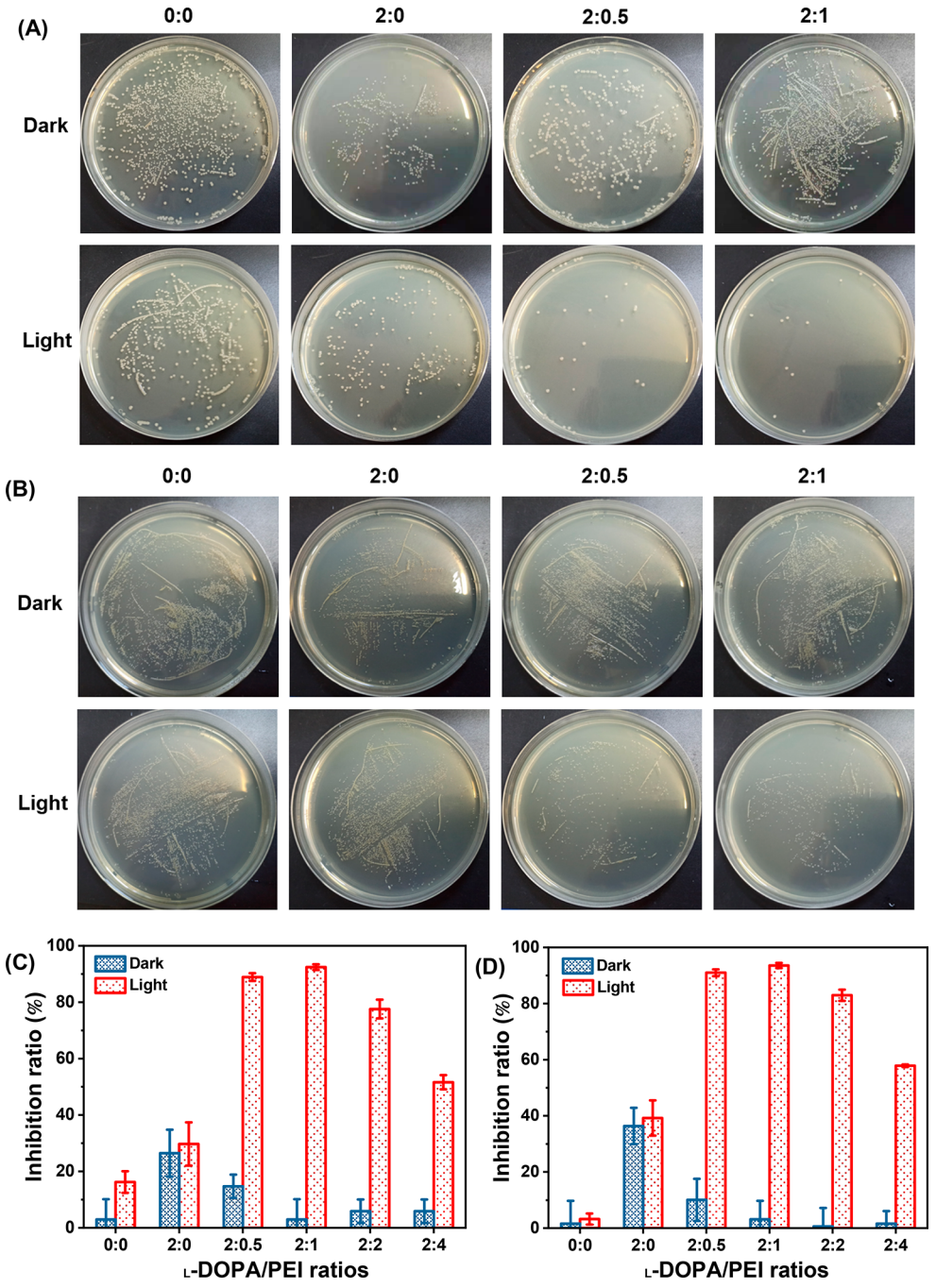

Figure 6. (A and B) Digital images of treated agar plates for photocatalytic antibacterial activity against *E. coli* and *S. aureus* treated with the studied *β*-FeOOH catalysts. (C and D) Photocatalytic antibacterial rate of the studied *β*-FeOOH catalysts against *E. coli* and *S. aureus*. (The mineralization time was kept at 2 h, and the sunlight irradiation time was kept at 20 min.)

Different types of dyes, including methylene blue, methyl blue, methyl orange, direct yellow, and rhodamine B, were used to evaluate the photodegradation efficiencies of the prepared catalysts (Figure 5C). The results indicate that the degradation efficiency reaches 99% within 60 min for all kinds of dyed wastewater. Furthermore, a cyclic photo-Fenton reaction was conducted to evaluate the durability of the *β*-FeOOH catalysts. As shown in Figure 5D, the degradation efficiency of methylene blue remains above 90% after five cycles of photodegradation. These results demonstrate that the *β*-FeOOH nanorods mineralized by L-DOPA-based coatings have good stability, which is advantageous for recycling applications.

The *β*-FeOOH catalysts can generate a large number of hydroxyl radicals through the photo-Fenton reaction, which is speculated to have photocatalytic bactericidal properties. *Escherichia coli* and *Staphylococcus aureus* were adopted as model Gram-negative and Gram-positive bacteria, respectively, for experiments. The antibacterial ability was evaluated using standard plate counting assays. As shown in Figure 6A,B and Figure S13 in the Supporting Information, the *β*-FeOOH catalysts with L-DOPA-based coatings can reduce the survival rate of bacteria under simulated sunlight. Figure 6C,D shows

https://doi.org/10.1021/acs.langmuir.2c00999
Langmuir 2022, 38, 9587−9596

that the β-FeOOH catalysts with L-DOPA-based coatings (2:1, light) significantly reduce the viability of *E. coli* and *S. aureus* by 93 and 94%, respectively, while those without the mussel-inspired coatings (0:0, light) eliminate bacteria by only 16 and 3%. The above results demonstrate that the introduction of the L-DOPA-based coatings can also greatly improve the photocatalytic sterilization performance of the Fenton catalysts.

CONCLUSIONS

We have developed a facile and effective strategy to achieve the rapid fabrication of porous Fenton catalysts by taking advantage of the strong chelation of carboxyl groups and catechol groups in L-DOPA-based mussel-inspired coatings to the Fe^{3+} in the β-FeOOH nanorods. Through the promotion of L-DOPA-based coatings, only 2 h of mineralization is required to fabricate β-FeOOH catalysts with excellent photocatalytic efficiency. Moreover, the L-DOPA-based coatings can effectively enhance the absorption of ultraviolet and visible light by the photocatalysts. Meanwhile, the indole structure (DHI and DHICA) in the coating also has good electron-transfer ability, which can reduce the electron−hole recombination rate and improve the electron-transport efficiency. The electron-delocalization ability of the carboxyl ligands in the L-DOPA-based coating effectively improves the energy band structure of the photocatalyst and further promotes the photo-Fenton reaction of β-FeOOH catalysts. Under simulated sunlight photocatalysis, the prepared β-FeOOH catalysts triggered by the L-DOPA-based coating exhibit a degradation efficiency for methyl blue dye of up to 99% within 30 min and a sterilization efficiency for *E. coli*/*S. aureus* of up to 93/94% within 20 min. Furthermore, the optimized catalysts exhibit high-efficiency photodegradation and good recyclability for various dyes, indicating the application potential for chemical and microbial pollutant treatment.

ASSOCIATED CONTENT

Supporting Information

The Supporting Information is available free of charge at https://pubs.acs.org/doi/10.1021/acs.langmuir.2c00999.

FESEM images, ATR/FT-IR spectra, XPS results, dynamic water contact angle, surface zeta potentials, UV−visible diffuse reflectance spectra, photoluminescence emission spectra, FL spectra of the different samples, and digital images of the photocatalytic performance of the catalysts for dye degradation and sterilization (PDF)

AUTHOR INFORMATION

Corresponding Authors

Jian Ji − *MOE Key Laboratory of Macromolecular Synthesis and Functionalization, and Key Laboratory of Adsorption and Separation Materials & Technologies of Zhejiang Province, Department of Polymer Science and Engineering, Zhejiang University, Hangzhou 310027, China; The "Belt and Road" Sino-Portugal Joint Laboratory on Advanced Materials, International Research Center for X Polymers, Zhejiang University, Hangzhou 310027, China;* orcid.org/0000-0001-9870-4038; Email: jijian@zju.edu.cn

Zhi-Kang Xu − *MOE Key Laboratory of Macromolecular Synthesis and Functionalization, and Key Laboratory of Adsorption and Separation Materials & Technologies of Zhejiang Province, Department of Polymer Science and Engineering, Zhejiang University, Hangzhou 310027, China; The "Belt and Road" Sino-Portugal Joint Laboratory on Advanced Materials, International Research Center for X Polymers, Zhejiang University, Hangzhou 310027, China;* orcid.org/0000-0002-2261-7162; Email: xuzk@zju.edu.cn

Authors

Shang-Jin Yang − *MOE Key Laboratory of Macromolecular Synthesis and Functionalization, and Key Laboratory of Adsorption and Separation Materials & Technologies of Zhejiang Province, Department of Polymer Science and Engineering, Zhejiang University, Hangzhou 310027, China; The "Belt and Road" Sino-Portugal Joint Laboratory on Advanced Materials, International Research Center for X Polymers, Zhejiang University, Hangzhou 310027, China*

Zhi-Yuan Xu − *MOE Key Laboratory of Macromolecular Synthesis and Functionalization, and Key Laboratory of Adsorption and Separation Materials & Technologies of Zhejiang Province, Department of Polymer Science and Engineering, Zhejiang University, Hangzhou 310027, China; The "Belt and Road" Sino-Portugal Joint Laboratory on Advanced Materials, International Research Center for X Polymers, Zhejiang University, Hangzhou 310027, China*

Ling-Yun Zou − *MOE Key Laboratory of Macromolecular Synthesis and Functionalization, and Key Laboratory of Adsorption and Separation Materials & Technologies of Zhejiang Province, Department of Polymer Science and Engineering, Zhejiang University, Hangzhou 310027, China; The "Belt and Road" Sino-Portugal Joint Laboratory on Advanced Materials, International Research Center for X Polymers, Zhejiang University, Hangzhou 310027, China*

Jiong-Chi Yu − *MOE Key Laboratory of Macromolecular Synthesis and Functionalization, and Key Laboratory of Adsorption and Separation Materials & Technologies of Zhejiang Province, Department of Polymer Science and Engineering, Zhejiang University, Hangzhou 310027, China; The "Belt and Road" Sino-Portugal Joint Laboratory on Advanced Materials, International Research Center for X Polymers, Zhejiang University, Hangzhou 310027, China;* orcid.org/0000-0002-2888-4499

Complete contact information is available at: https://pubs.acs.org/10.1021/acs.langmuir.2c00999

Author Contributions

§S.-J.Y., Z.-Y.X., and L.-Y.Z. contributed equally.

Notes

The authors declare no competing financial interest.

ACKNOWLEDGMENTS

This work is financially supported by the National Natural Science Foundation of China (grant no. 51673166).

REFERENCES

(1) Vörösmarty, C. J.; McIntyre, P. B.; Gessner, M. O.; Dudgeon, D.; Prusevich, A.; Green, P.; Glidden, S.; Bunn, S. E.; Sullivan, C. A.; Liermann, C. R.; et al. Global threats to human water security and river biodiversity. *Nature* **2010**, *467* (7315), 555−561.

(2) Saravanan, A.; Senthil Kumar, P.; Jeevanantham, S.; Karishma, S.; Tajsabreen, B.; Yaashikaa, P. R.; Reshma, B. Effective water/wastewater treatment methodologies for toxic pollutants removal:

Processes and applications towards sustainable development. *Chemosphere* **2021**, *280*, 130595.
(3) Thomas, N.; Dionysiou, D. D.; Pillai, S. C. Heterogeneous Fenton catalysts: A review of recent advances. *J. Hazard. Mater.* **2021**, *404*, 124082.
(4) Ling, S.; Qin, Z.; Huang, W.; Cao, S.; Kaplan, D. L.; Buehler, M. J. Design and function of biomimetic multilayer water purification membranes. *Sci. Adv.* **2017**, *3* (4), No. e1601939.
(5) Haque, E.; Jun, J. W.; Jhung, S. H. Adsorptive removal of methyl orange and methylene blue from aqueous solution with a metal-organic framework material, iron terephthalate (MOF-235). *J. Hazard. Mater.* **2011**, *185* (1), 507−511.
(6) Yu, C.; Li, G.; Kumar, S.; Yang, K.; Jin, R. Phase transformation synthesis of novel Ag_2O/Ag_2CO_3 heterostructures with high visible light efficiency in photocatalytic degradation of pollutants. *Adv. Mater.* **2014**, *26* (6), 892−898.
(7) Marin, M. L.; Santos-Juanes, L.; Arques, A.; Amat, A. M.; Miranda, M. A. Organic photocatalysts for the oxidation of pollutants and model compounds. *Chem. Rev.* **2012**, *112* (3), 1710−1750.
(8) Wang, W.; Xie, C.; Zhu, L.; Shan, B.; Liu, C.; Cui, F. A novel 3-dimensional graphene-based membrane with superior water flux and electrocatalytic properties for organic pollutant degradation. *J. Mater. Chem. A* **2019**, *7* (1), 172−187.
(9) Lotito, A. M.; Fratino, U.; Bergna, G.; Di Iaconi, C. Integrated biological and ozone treatment of printing textile wastewater. *Chem. Eng. J.* **2012**, *195*−*196*, 261−269.
(10) Aravind, P.; Selvaraj, H.; Ferro, S.; Sundaram, M. An integrated (electro- and bio-oxidation) approach for remediation of industrial wastewater containing azo-dyes: Understanding the degradation mechanism and toxicity assessment. *J. Hazard. Mater.* **2016**, *318*, 203−215.
(11) Liu, Y.; Zhao, Y.; Wang, J. Fenton/Fenton-like processes with in-situ production of hydrogen peroxide/hydroxyl radical for degradation of emerging contaminants: Advances and prospects. *J. Hazard. Mater.* **2021**, *404*, 124191.
(12) Qin, Y.; Zhang, L.; An, T. Hydrothermal carbon-mediated Fenton-like reaction mechanism in the degradation of alachlor: direct electron transfer from hydrothermal carbon to Fe(III). *ACS Appl. Mater. Interfaces* **2017**, *9* (20), 17115−17124.
(13) Hao, S.-M.; Qu, J.; Zhu, Z.-S.; Zhang, X.-Y.; Wang, Q.-Q.; Yu, Z.-Z. Hollow manganese silicate nanotubes with tunable secondary nanostructures as excellent fenton-type catalysts for dye decomposition at ambient temperature. *Adv. Funct. Mater.* **2016**, *26* (40), 7334−7342.
(14) Zhou, X.; Lan, J.; Liu, G.; Deng, K.; Yang, Y.; Nie, G.; Yu, J.; Zhi, L. Facet-mediated photodegradation of organic dye over hematite architectures by visible light. *Angew. Chem., Int. Ed.* **2012**, *51* (1), 178−182.
(15) Ganiyu, S. O.; Zhou, M.; Martínez-Huitle, C. A. Heterogeneous electro-Fenton and photoelectro-Fenton processes: A critical review of fundamental principles and application for water/wastewater treatment. *Appl. Catal. B Environ.* **2018**, *235*, 103−129.
(16) Zhang, S.; Gao, H.; Huang, Y.; Wang, X.; Hayat, T.; Li, J.; Xu, X.; Wang, X. Ultrathin g-C_3N_4 nanosheets coupled with amorphous Cu-doped FeOOH nanoclusters as 2D/0D heterogeneous catalysts for water remediation. *Environ. Sci.: Nano* **2018**, *5* (5), 1179−1190.
(17) Liu, J.; Xie, S.; Geng, Z.; Huang, K.; Fan, L.; Zhou, W.; Qiu, L.; Gao, D.; Ji, L.; Duan, L.; et al. Carbon nitride supramolecular hybrid material enabled high-efficiency photocatalytic water treatments. *Nano Lett.* **2016**, *16* (10), 6568−6575.
(18) Chen, Y.; Zhang, G.; Liu, H.; Qu, J. Confining free radicals in close vicinity to contaminants enables ultrafast Fenton-like processes in the interspacing of MoS_2 membranes. *Angew. Chem., Int. Ed.* **2019**, *58* (24), 8134−8138.
(19) Shi, L.; Shi, Y.; Zhuo, S.; Zhang, C.; Aldrees, Y.; Aleid, S.; Wang, P. Multi-functional 3D honeycomb ceramic plate for clean water production by heterogeneous photo-Fenton reaction and solar-driven water evaporation. *Nano Energy* **2019**, *60*, 222−230.
(20) Nidheesh, P. V. Heterogeneous Fenton catalysts for the abatement of organic pollutants from aqueous solution: a review. *RSC Adv.* **2015**, *5* (51), 40552−40577.
(21) Lv, Y.; Zhang, C.; He, A.; Yang, S.-J.; Wu, G.-P.; Darling, S. B.; Xu, Z.-K. Photocatalytic nanofiltration membranes with self-cleaning property for wastewater treatment. *Adv. Funct. Mater.* **2017**, *27* (27), 1700251.
(22) Zhang, C.; Yang, H.-C.; Wan, L.-S.; Liang, H.-Q.; Li, H.; Xu, Z.-K. Polydopamine-coated porous substrates as a platform for mineralized β-FeOOH nanorods with photocatalysis under sunlight. *ACS Appl. Mater. Interfaces* **2015**, *7* (21), 11567−11574.
(23) Yang, S.-J.; Zou, L.-Y.; Liu, C.; Zhong, Q.; Ma, Z.-Y.; Yang, J.; Ji, J.; Müller-Buschbaum, P.; Xu, Z.-K. Codeposition of levodopa and polyethyleneimine: Reaction mechanism and coating construction. *ACS Appl. Mater. Interfaces* **2020**, *12* (48), 54094−54103.
(24) Wang, W.; Sun, J.; Zhang, Y.; Zhang, Y.; Hong, G.; Moutloali, R. M.; Mamba, B. B.; Li, F.; Ma, J.; Shao, L. Mussel-inspired tannic acid/polyethyleneimine assembling positively-charged membranes with excellent cation permselectivity. *Sci. Total Environ.* **2022**, *817*, 153051.
(25) Filippidi, E.; Cristiani, T. R.; Eisenbach, C. D.; Waite, J. H.; Israelachvili, J. N.; Ahn, B. K.; Valentine, M. T. Toughening elastomers using mussel-inspired iron-catechol complexes. *Science* **2017**, *358* (6362), 502.
(26) Holten-Andersen, N.; Harrington, M. J.; Birkedal, H.; Lee, B. P.; Messersmith, P. B.; Lee, K. Y.; Waite, J. H. pH-induced metal-ligand cross-links inspired by mussel yield self-healing polymer networks with near-covalent elastic moduli. *Proc. Natl. Acad. Sci. U.S.A.* **2011**, *108* (7), 2651−2655.
(27) Harrington, M. J.; Masic, A.; Holten-Andersen, N.; Waite, J. H.; Fratzl, P. Iron-clad fibers: A metal-based biological strategy for hard flexible coatings. *Science* **2010**, *328* (5975), 216.
(28) Sever, M. J.; Wilker, J. J. Absorption spectroscopy and binding constants for first-row transition metal complexes of a DOPA-containing peptide. *Dalton Trans.* **2006**, No. 6, 813−822.
(29) Panzella, L.; Gentile, G.; D'Errico, G.; Della Vecchia, N. F.; Errico, M. E.; Napolitano, A.; Carfagna, C.; d'Ischia, M. Atypical structural and π-electron features of a melanin polymer that lead to superior free-radical-scavenging properties. *Angew. Chem., Int. Ed.* **2013**, *52* (48), 12684−12687.
(30) Kim, J. H.; Lee, M.; Park, C. B. Polydopamine as a biomimetic electron gate for artificial photosynthesis. *Angew. Chem., Int. Ed.* **2014**, *53* (25), 6364−6368.
(31) Dimitrijevic, N. M.; Rozhkova, E.; Rajh, T. Dynamics of localized charges in dopamine-modified TiO_2 and their effect on the formation of reactive oxygen species. *J. Am. Chem. Soc.* **2009**, *131* (8), 2893−2899.
(32) Ahile, U. J.; Wuana, R. A.; Itodo, A. U.; Sha'Ato, R.; Dantas, R. F. A review on the use of chelating agents as an alternative to promote photo-Fenton at neutral pH: Current trends, knowledge gap and future studies. *Sci. Total Environ.* **2020**, *710*, 134872.
(33) Lettieri, S.; Pavone, M.; Fioravanti, A.; Santamaria Amato, L.; Maddalena, P. Charge carrier processes and optical properties in TiO_2 and TiO_2-based heterojunction photocatalysts: A review. *Materials* **2021**, *14* (7), 1645.
(34) Cuerda-Correa, E. M.; Alexandre-Franco, M. F.; Fernández-González, C. Advanced oxidation processes for the removal of antibiotics from water. An overview. *Water* **2020**, *12* (1), 102.
(35) Kamat, P. V. Boosting the efficiency of quantum dot sensitized solar cells through modulation of interfacial charge transfer. *Acc. Chem. Res.* **2012**, *45* (11), 1906−1915.
(36) Chen, X.; Liu, L.; Yu Peter, Y.; Mao Samuel, S. Increasing solar absorption for photocatalysis with black hydrogenated titanium dioxide nanocrystals. *Science* **2011**, *331* (6018), 746−750.
(37) Wang, S.; Zhao, L.; Bai, L.; Yan, J.; Jiang, Q.; Lian, J. Enhancing photocatalytic activity of disorder-engineered C/TiO_2 and TiO_2 nanoparticles. *J. Mater. Chem. A* **2014**, *2* (20), 7439−7445.

https://doi.org/10.1021/acs.langmuir.2c00999
Langmuir 2022, 38, 9587−9596

(38) Xiang, Q.; Yu, J.; Wong, P. K. Quantitative characterization of hydroxyl radicals produced by various photocatalysts. *J. Colloid Sci.* **2011**, *357* (1), 163−167.
(39) Bai, S.; Zhang, N.; Gao, C.; Xiong, Y. Defect engineering in photocatalytic materials. *Nano Energy* **2018**, *53*, 296−336.

https://doi.org/10.1021/acs.langmuir.2c00999
Langmuir 2022, 38, 9587−9596